Available online at www.sciencedirect.com

ScienceDirect

Geochimica et Cosmochimica Acta 188 (2016) 310–329

Geochimica et Cosmochimica Acta

www.elsevier.com/locate/gca

Evaluation of mineral reactive surface area estimates for prediction of reactivity of a multi-mineral sediment

Lauren E. Beckingham [a,*,1], Elizabeth H. Mitnick [b], Carl I. Steefel [a], Shuo Zhang [b], Marco Voltolini [a], Alexander M. Swift [c], Li Yang [a], David R. Cole [c], Julia M. Sheets [c], Jonathan B. Ajo-Franklin [a], Donald J. DePaolo [a,b], Saeko Mito [d], Ziqiu Xue [d]

[a] *Lawrence Berkeley National Laboratory, 1 Cyclotron Rd., Berkeley, CA 94720, USA*
[b] *University of California, Berkeley, Earth and Planetary Science, Berkeley, CA 94720, USA*
[c] *The Ohio State University, 275 Mendenhall Lab, 125 South Oval Mall, Columbus, OH 43210, USA*
[d] *Research Institute of Innovative Technology for the Earth (RITE), 9-2, Kizugawadai, Kizugawa-Shi, Kyoto 619-0292, Japan*

Received 24 October 2015; accepted in revised form 25 May 2016; available online 4 June 2016

Abstract

Our limited understanding of mineral reactive surface area contributes to significant uncertainties in quantitative simulations of reactive chemical transport in subsurface processes. Continuum formulations for reactive transport typically use a number of different approximations for reactive surface area, including geometric, specific, and effective surface area. In this study, reactive surface area estimates are developed and evaluated for their ability to predict dissolution rates in a well-stirred flow-through reactor experiment using disaggregated samples from the Nagaoka pilot CO_2 injection site (Japan). The disaggregated samples are reacted with CO_2 acidified synthetic brine under conditions approximating the field conditions and the evolution of solute concentrations in the reactor effluent is tracked over time. The experiments, carried out in fluid-dominated conditions at a pH of 3.2 for 650 h, resulted in substantial dissolution of the sample and release of a disproportionately large fraction of the divalent cations. Traditional reactive surface area estimation methods, including an adjusted geometric surface area and a BET-based surface area, are compared to a newly developed image-based method. Continuum reactive transport modeling is used to determine which of the reactive surface area models provides the best match with the effluent chemistry from the well-stirred reactor. The modeling incorporates laboratory derived mineral dissolution rates reported in the literature and the initial modal mineralogy of the Nagaoka sediment was determined from scanning electron microscopy (SEM) characterization. The closest match with the observed steady-state effluent concentrations was obtained using specific surface area estimates from the image-based approach supplemented by literature-derived BET measurements. To capture the evolving effluent chemistry, particularly over the first 300 h of the experiment, it was also necessary to account for the grain size distribution in the sediment and the presence of a highly reactive volcanic glass phase that shows preferential cation leaching.

Keywords: Reactive surface area; CO_2 sequestration; Mineral reaction rates

* Corresponding author at: Department of Civil Engineering, Auburn University, Auburn, AL 36830, USA. Tel.: +1 334 844 6260.
E-mail address: leb@auburn.edu (L.E. Beckingham).
[1] Current address: Auburn University, 211 Harbert Engineering Center, Auburn, AL 36830, USA.

http://dx.doi.org/10.1016/j.gca.2016.05.040
0016-7037/

1. INTRODUCTION

Reactive transport modeling is a powerful approach for predicting the physical and chemical evolution of natural porous media systems (Steefel et al., 2005). Accurate predictions, however, require a quantitative treatment of mineral dissolution and precipitation reactions. A good example is the problem of mineral trapping associated with subsurface CO_2 injection and sequestration (Gaus, 2010; Pham et al., 2011; Hellevang et al., 2013). The coupled dissolution and precipitation rates determine the time scales required for mineral trapping, but also modify the pore structure and pore- and pore-throat size distributions and connectivities (eg. Crandell et al., 2012). Rigorous modeling of these pore scale mineralogical processes is needed as they directly impact processes and parameters at larger scales, including permeability evolution (Beckingham et al., 2013; Nogues et al., 2013).

Mineral dissolution and precipitation reactions are typically slow in comparison to geologic CO_2 sequestration (GCS) injection time scales and the kinetics of these reactions need to be treated explicitly in quantitative numerical models for water–gas–rock interaction to predict long-term performance of the storage system. At present, the ability of continuum reactive transport models to accurately predict mineral reaction rates is limited (Black et al., 2015; Bourg et al., 2015), although there are some successes (Maher et al., 2009; Noiriel et al., 2012). One of the principal uncertainties in modeling mineral reaction rates comes from estimation of mineral reactive surface area rather than intrinsic rate values (Bourg et al., 2015; Wigley et al., 2013; Zhu and Lu, 2013). This limitation results in discrepancies in predicted pore structure evolutions (summarized in Gaus et al., 2008), amounts of secondary mineral precipitation (Hellevang and Aagaard, 2013; Bolourinejad et al., 2014), and the timescale of (trapping) reactions (Xu et al., 2014). Similar uncertainties are associated with the modeling of water–rock interaction processes in other environments, including marine diagenesis (Maher et al., 2006), chemical weathering (Maher et al., 2009; Navarre-Sitchler et al., 2011), contaminant fate and transport (Li et al., 2009), and geological nuclear waste repository performance (Marty et al., 2015).

The term "reactive surface area" or "RSA" as defined here is primarily a concept (and thus a parameter) that is used in continuum reactive transport models (Steefel et al., 2015a). In the continuum treatment of water–rock and water-soil processes, a representative elementary volume (REV) is defined that consists of an assortment of mineral grains packed together with some pore structure. Individual reactive sites and even individual mineral surfaces in the continuum approach are not normally resolved (Molins, 2015). Instead, average values (Maher et al., 2009) or a distribution of values (Liu et al., 2015) are used (Fig. 1). This approximation is necessary because the detailed reactive site distribution is not available in natural systems as it may be on a single mineral grain in an Atomic Force Microscopy (AFM) study (Teng et al., 2000; Bracco et al., 2013). The total reactive surface area used in continuum scale reactive transport models serves as a proxy for the actual concentration of reactive sites on the mineral. However, in conventional experimental rate determinations (e.g., a well-mixed flow-through reactor), the rate is normalized to the physical surface area (e.g., through the use of a BET determination) and the site density is assumed to be implicit in the rate constant.

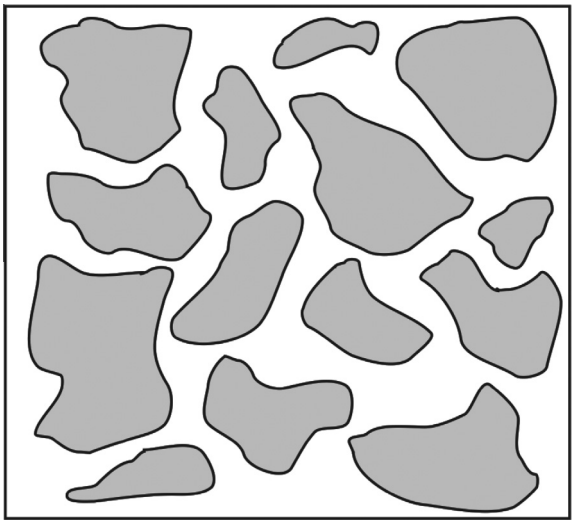

Fig. 1. Schematic representation of a representative elementary volume (REV) in a continuum reactive transport model. In the continuum approximation for mineral reaction, an average value for the reactive surface area is used.

Currently, the commonly utilized reactive transport models used to describe fate and transport in subsurface materials (Steefel et al., 2015b) make use of a single value of the reactive surface area that is intended to capture the average reactivity of each mineral phase, A_m (m^2 mineral/m^3 porous medium), according to Steefel and Lasaga (1994):

$$R_m = A_m k[f\Delta G_r] \quad (1)$$

where k is the rate constant and $f\Delta G_r$ is some function of Gibbs free energy, or the thermodynamic driving force for the reaction. The bulk reactive surface area, A_m, is related to the more typically measured specific surface area by,

$$A_m = (\mathrm{SSA} \cdot \phi_m \cdot M_w \cdot V_m^{-1}) \quad (2)$$

where SSA is the specific surface area of the mineral (m^2/g), ϕ_m is the mineral volume fraction (m^3 mineral/m^3 porous medium), M_w is its molecular weight (g/mol), and V_m is the molar volume (m^3/mol).

Currently, there is no universally accepted method for estimating average mineral reactive surface areas. Consequently, a range of approximations have been developed based on easily measurable attributes. The goal of this work is to evaluate these reactive surface area approximations on mineral dissolution rates by comparison between modeling and experimental results. The simplest approach estimates reactive surface area as geometric surface area (GSA), assuming a single grain diameter and spherical or cubic geometry for all minerals (Steefel and Lasaga, 1994; Steefel and Lichtner, 1998; Gunter et al., 2000) or two distinct grain diameters, one for clay minerals and one for

all other minerals (Xu et al., 2004; White et al., 2005; Alemu et al., 2011). An alternative approach is to add a crystal size distribution to calculate a total surface area for the reactive phase (Steefel and Van Cappellen, 1990). In many cases, GSA estimates assume an ideal geometry and do not account for surface roughness, although introducing an average value for the surface roughness is straightforward (Zerai et al., 2006; White et al., 2008; Maher et al., 2009; Zhang et al., 2009). With the roughness factor (RF), with RF >1, the surface area reflects the total surface area of the mineral, which when normalized to the mass of mineral becomes the specific surface area (or SSA, Table 1). The normalized specific surface area can also be measured in the laboratory using the Brunauer, Emmett, Teller (BET) method (Brunauer et al., 1938).

Mineral dissolution and precipitation rates may be overestimated in laboratory experiments compared to natural environments because they use mineral samples with highly reactive surfaces, in contrast to lower reactive surfaces often observed in natural samples (Noiriel et al., 2012). In these cases, a scaling factor (SF, where $SF = 10^{-x}$ with x typically 1–3) may be applied to account for the reduced surface reactivity. These large scaling factors are difficult to reconcile with reactive site density effects alone and probably reflect porous medium effects having to do with the accessibility of reactive surfaces to the connected pore structure (Peters, 2009; Landrot et al., 2012), or diffusion control including diffusive boundary layer effects (Pokrovsky and Schott, 2000; Noiriel et al., 2012). This effect should not be significant in this study, however, because the samples are disaggregated.

In what follows, we distinguish between two approximations for reactive surface area: (1) specific surface area (SSA) determined based either on geometry (GSA, either assumed ideal or derived from image analysis), or (2) effective surface area (ESA) that accounts for the effects of surface site reactivity, pore accessibility, and diffusion control (Table 1). Note that both the GSA and ESA have units of specific surface area (m^2 mineral/g mineral). While some studies have made rigorous efforts to determine the appropriate roughness and scaling factors to be used (Maher et al., 2009; Lai et al., 2015), many modeling studies use 'typical values' that are largely arbitrary. This introduces order(s) of magnitude ranges of surface areas and as much as five orders of magnitude variation in mineral reactive surface areas have been used in field-scale GCS modeling alone, as illustrated in Bourg et al. (2015).

Table 1
Summary of surface area terminology and typical laboratory or computational approaches.

Approximations of reactive surface area	Description
Specific surface area (SSA)	Geometric surface area (GSA) based on ideal geometry, computed with or without a surface roughness factor
	Image perimeter based SSA
	BET surface area, laboratory measured using BET analysis
Effective surface area (ESA)	Accounts for surface site reactivity, pore accessibility, or diffusion control. May be computed by applying a scaling factor (SF) to SSA

In this study, we evaluate mineral reactive surface area approximations and their ability to provide accurate simulations of dissolution rates for samples from the Nagaoka pilot CO_2 injection site. Mineral reactive surface areas were determined from traditional and novel image based approaches. Traditional approaches included calculation of an adjusted GSA, BET measurement of total sample SSA, and compilation of BET measurements of pure mineral SSA from existing literature. A new image analysis method was developed to estimate phase-specific mineral surface areas from 2D grain perimeters in SEM images. To determine which of the reactive surface area approximations was best, we carried out a flow-through disaggregated Nagaoka sediment dissolution rate experiment and compared the observed effluent chemistry with the results of reactive transport modeling based on the various RSA formulations. Rate constants for dissolution as a function of temperature, pH, and pCO_2 were based on intrinsic rates reported in the literature.

2. METHODS

2.1. Materials

Reservoir rock samples used in this study were subsampled from whole core acquired from observation well OB-2 at the Nagaoka pilot CO_2 injection site in Japan (Mito et al., 2008). Before supercritical CO_2 ($scCO_2$) injection started, cores were extracted from a depth of 1093 m, corresponding to the target zone for injection in the Pleistocene Haizume formation (Mito et al., 2008). The reservoir rock is a moderately poorly sorted immature volcanic fine sand, or greywacke, with a typical grain size in the range of 50–200 μm with thin layers of interbedded siltstone and mudstone (Chiyonobu et al., 2013). The clast population contains substantial fractions of calcic plagioclase and pyroxene, lithic volcanic clasts, and volcanic glass or devitrified glass. Compared to most reservoirs rocks used for CO_2 injection experiments, this formation has a much higher fraction of more reactive minerals and rock fragments, and hence has the characteristics necessary to promote CO_2 mineralization (eg. Zhang et al., 2013).

2.2. Mineralogical analysis

The identity of various mineral phases in the sample was determined using X-ray powder diffraction (XRD), SEM imaging, and X-ray fluorescence (XRF) analysis. The XRD analysis was performed on a small fragment collected from the hand sample, powdered in a mortar. The measurement was carried out with a Rigaku SmartLab® diffractometer (40 kV, 30 mA) using Cu Kα radiation. Quantitative phase analysis was carried out with the software MAUD (Lutterotti et al., 1997) using a Rietveld

quantitative phase analysis procedure (McCusker et al., 1999). Phases used in the analysis were obtained from either the ICDD database or the COD database (http://www.crystallography.net/). Instrumental parameters were refined using a corundum standard; background, scale factors and preferred orientation were refined (along with phase-dependent profile shape function parameters for the main phases), and for the smectite phase turbostratical disorder was modeled as well (Lutterotti et al., 2010). This analysis identified the crystalline phases as predominantly quartz (37.3 wt%), smectite (25.6 wt%), plagioclase (19.7 wt%), and K-feldspar (11.5 wt%) with the complete analysis in Table 2. This is broadly consistent with mineral proportions reported in Mito et al. (2008).

XRD was also used to calculate the fraction of amorphous material in the sample via a Rietveld + RIR ("Reference Intensity Ratio") approach (Gualtieri, 2000). The powdered rock sample was used to prepare different samples mixed with 30% and 60% (by weight) standard corundum powder, then a Rietveld analysis was performed on the different XRD profiles. The resulting plot of the measured vs. actual weight% of the standard indicated the presence of 8.5% amorphous material in the sample. In this sample the amorphous phases consists of glass and clays. Clays in this sample display a poor crystallinity, and even if during the analysis of the diffraction patterns the most advanced models of crystallinity and structural disorder have been employed, some diffuse scattering that is not able to be modeled is present.

X-ray fluorescence (XRF) on the bulk rock was performed as an additional confirmation of the minerals identified in the 2D SEM imaging (described below in Section 2.3). This analysis, carried out using a ThermoARL Advant'XP by the Peter Hooper GeoAnalytical Lab at Washington State University (http://environment.wsu.edu/facilities/geolab/), provides the rock composition in weight percent oxides (given in Appendix A). To compute mineral weight percent distribution, it was assumed that the minor mineral phases were present in the same quantities as determined by 2D SEM imaging (Section 2.3). These include biotite, amphibole, Fe Hydroxide, chlorite, kaolinite, pyrite, serpentine, and calcite, each contributing less than 3 wt% each for a total of 9.1 wt%. The distribution of major mineral phases that contributed 90.9 wt%, was then calculated using a linear least squares approach with non-negativity constraints. The corresponding distribution of major mineral phases is given in Table 2 and agrees well with the XRD analysis.

Table 2
Mineral distribution by weight percent as determined from XRD and XRF analysis.

Mineral	wt%, XRD	wt%, XRF
Quartz	37.3	21.4
Plagioclase	19.7	21.3
K-feldspar	11.5	10.3
Smectite	25.6	28.9
Pyroxene	5.5	8.9
Kaolinite	<1	
Spinel	<1	

2.3. 2D SEM imaging

A polished thin section was made from an epoxy-impregnated Nagaoka core sample for 2D SEM imaging. High-resolution SEM backscattered electron (BSE) images were collected using a FEI Quanta 250 Field Emission Gun (FEG) SEM at Subsurface Energy Materials Characterization and Analysis Laboratory (SEMCAL), School of Earth Sciences, The Ohio State University. Images were obtained using an accelerating voltage of 15.00 keV and a working distance of 13.6 mm. Images were acquired with a pixel resolution of 0.2 μm. Image stitching resulted in the final 17,856 × 24,572 pixel (16.9 mm^2) image interpreted in this study. Segmentation of the final BSE image (Fig. 2B) into pore and grain pixels was performed using the threshold optimization method described in Peters (2009). The corresponding pore-grain threshold value was 45 on a scale of grayscale intensities ranging from 0 to 255 (Fig. 2A). Further details on image segmentation can be found in Appendix B.

The SEM used in this study is also equipped for electron dispersive spectroscopy analysis using the Quantitative Evaluation of Minerals by SCANning electron microscopy (QEMSCAN®) mineral processing software. QEMSCAN® images were acquired at 25 keV and 10 nA specimen current, using a pixel resolution of 2.5 × 2.5 microns on the same area as the high-resolution BSE images. QEMSCAN® processes the BSE signal intensity, along with 1000 counts of characteristic X-rays (detected with a Bruker X'Flash energy dispersive X-ray spectrometer) for each point analyzed. Using FEI mineral standards acquired under the same experimental conditions, the corresponding mineral in the sample was identified based on mineral-specific rules for elements and peak heights, ratios of elements, and the BSE value. Mineral identification standards were adjusted until reasonable results were obtained, based on good agreement with the XRD analysis and grain morphologies observed in the BSE images. Attempts were made to minimize grain edge effects, unclassified pixels, and pixels representing mixed signals where the beam interrogates mineral grain boundaries. This required an iterative series of adjustments of individual mineral identification tests. The final set of minerals was used to provide the modal mineral composition of the sample (Table 3). The BSE and QEMSCAN ® images were co-registered to create a 0.2 micron-resolution 2D image with mineral identities. Registration was performed using the BUnwarpJ plug-in for ImageJ (Arganda-Carreras et al., 2008).

2.4. Surface area characterization methods

2.4.1. Specific surface area from BET

BET measurements of pure mineral samples were obtained from existing experimental mineral dissolution rate studies in the literature. A compilation of BET measurements for each mineral was created and the low and high surface area measurements reported here. Given the large number of existing mineral dissolution rate experiments, the values reported here are representative of low and high values and do not necessarily correspond to the exact minimum or maximum values that can be found in the literature.

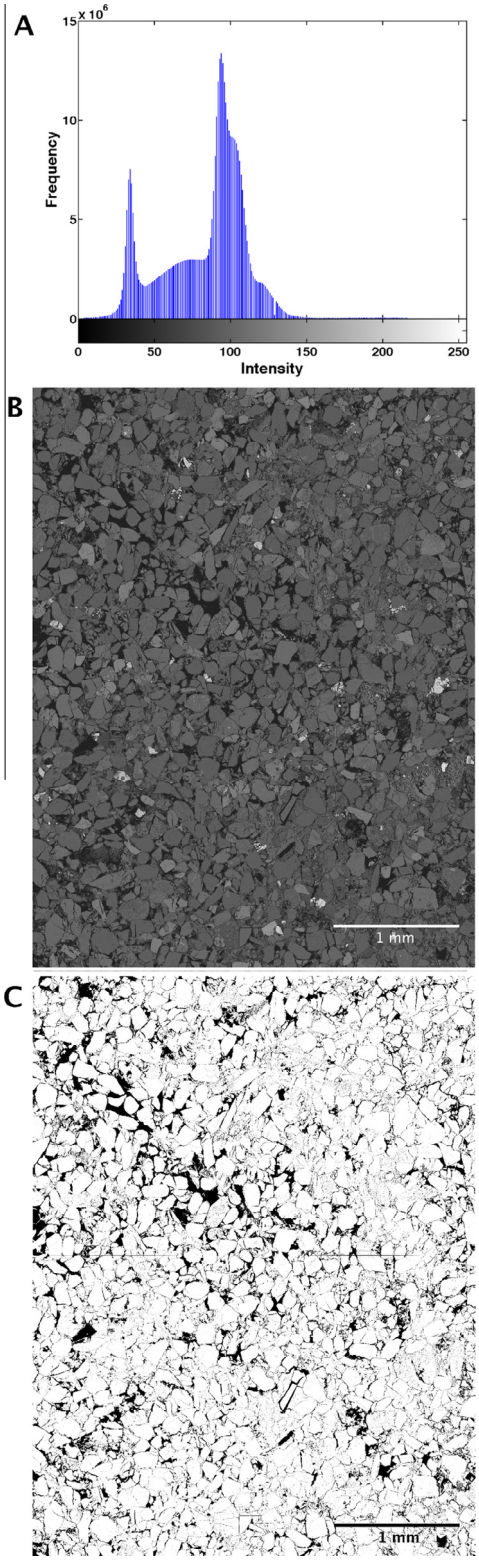

Fig. 2. Histogram of gray scale intensities (A) for SEM image (B) and corresponding segmented threshold image (C) with pores shown in black and grains in white.

The BET specific surface area of the Nagaoka reservoir samples were also measured using an Autosorb-1 surface area analyzer (Quantachrome instrument) with nitrogen as adsorption gas. Before the measurement, the Nagaoka core samples were carefully broken down into loose particles without extensive grinding to avoid artificially increasing the sample surface area, hence their description as "disaggregated" rather than "powdered". The sample prepared thereafter was degassed at 100 °C for 4 h and mounted on the instrument for surface area analysis. The specific surface area of the sample was determined by a 5 point BET analysis according to the classical Brunauer, Emmett and Teller equation (Brunauer et al., 1938).

2.4.2. Image perimeter specific surface areas from 2D image analysis

Mineral specific surface areas were computed from the 2D registered image by computing the perimeter of each discrete mineral grain in the 2D map using a Matlab script written for this purpose. Mineral perimeter densities were then computed by dividing by the area fraction of each mineral, where the area fractions were calculated by dividing the pixels of each mineral by the total number of image pixels. Based on principles originating in stereology, 3D surface area densities (surface area over volume) can be computed from 2D perimeter densities (perimeter over area) using a bias correction factor (Weibel, 1979). Applying the bias correction factor for spheres of $4/\pi$ mineral specific surface area densities were computed in units of mm^2/mm^3. By multiplying by the density of each mineral, surface areas in traditional units of m^2/g were determined. This provides an estimate of specific surface area since it includes surface roughness, albeit at the resolution of the 2D images.

This analysis can only be used to estimate the surface area of non-clay minerals. While the 2D images have a high resolution, they cannot capture the nano-scale features of clay minerals. The surface area of all clays and phyllosilicates except for smectite, were set to their high-range BET values from the literature examples (see Section 2.4.1). The surface area of smectite, the most abundant clay mineral, was computed by fitting the total sample surface area to the laboratory BET surface area measured here (see Section 2.4.1).

2.4.3. Effective surface area from scaled image perimeter specific surface area

The approach developed above (Section 2.4.2) provides an estimate of mineral specific surface areas. Frequently, scaling factors are applied to specific surface areas to account for the reactivity of surface sites, as discussed above. These effective surface areas are commonly computed using unconstrained scaling factors that may be as high as one to three orders of magnitude (see Section 1). To evaluate the effectiveness of this surface reactivity scaling approach, effective surface areas were computed from the image-obtained specific surface areas using a scaling factor of one order of magnitude. While recently there have been more rigorous approaches to adjust for surface site reactivity, this scaling factor was selected to evaluate the implication of applying even the most conservative (if unconstrained) scaling factor.

Table 3
Mineral volume fractions from image analysis and surface areas (m^2/g) as determined from the suite of traditional and new imaging methods. Example BET data for the low and high range of a literature search (low BET, high BET): quartz (Tester et al., 1994; Brady and Walther, 1990), albite (Stillings and Brantley, 1995; Gudbrandsson et al., 2014), Plag-An25 (Stillings and Brantley, 1995; Casey et al., 1991), Plag-An65 (Oelkers and Schott, 1995; Casey et al., 1991), smectite (Metz et al., 2005), K-feldspar (Stillings and Brantley, 1995; Bevan and Savage, 1989), Pyro-En60 (Oelkers and Schott, 2001), Pyro-En38 (Daval et al., 2010; Stockmann et al., 2013), biotite (Acker and Bricker, 1992; Hodson, 2006), amphibole (Schott et al., 1981; Frogner and Schweda, 1998), chlorite (Domenech et al., 2002; Black and Haese, 2014), kaolinite (Devidal et al., 1997; Wieland and Stumm, 1992), pyrite (Descostes et al., 2004; Domenech et al., 2002), serpentine (Park and Fan, 2004; Daval et al., 2013a), and calcite (Walter and Morse, 1984; Plummer and Wigley, 1976).

Mineral	Volume (%)	Lit. BET grain size range (μm)	Specific surface area			Effective surface area	
			BET of pure minerals, low lit. example (m^2/g)	BET of pure minerals, high lit. example (m^2/g)	Image perimeter SSA, smectite fit to BET[a] (m^2/g)	Image perimeter SSA, scaling factor 1 OM (m^2/g)	Scaled GSA,[b] smooth spheres, ESA = 3/r (m^2/g)
Quartz	27.64	75–850	0.0225	0.111	0.089	0.0089	0.0091
Plagioclase	21.4	25–150	0.04	0.645	0.109	0.0109	0.0091
Albite	6.46	75–150	0.04	0.164			0.0091
An25	1.49	75–100	0.088	0.645			0.0091
Labradorite	13.46	25–100	0.0414	0.52			0.0091
Smectite	16.99	0.1–150	34	97	136.3	13.63	0.64
K-feldspar	14.62	75–250	0.16	0.474	0.146	0.0146	0.0091
Pyroxene	7.21	50–500	0.028	0.105	0.214	0.0214	0.0091
Fe,Mg rich	5.46	50–100	0.08	0.088			0.0091
Ca,Mg rich	1.72	50–500	0.028	0.125			0.0091
AlSitrap	2.74				0.482	0.0482	0.0091
Biotite	2.58	10–420	0.51	4.74	4.74	0.474	0.64
Amphibole	1.85	75–250	0.005	0.28	0.234	0.0234	0.0091
Others	1.42				0.498	0.0498	0.0091
Fe Hydroxide	1.22				0.195	0.0195	0.0091
Chlorite	1.17	10–250	2.8	7.6	7.6	0.76	0.64
Kaolinite	0.41	5–100	3.17	13.2	13.2	1.32	0.64
Pyrite	0.36	10–250	0.03	1.1	0.149	0.0149	0.0091
Serpentine	0.29	37–800	4.6	7.15	7.15	0.715	0.64
Ca-phosphate	0.07				0.274	0.0274	0.0091
Calcite	0.03	44–81	0.03	0.5586	0.281	0.0281	0.0091
Total SA			5.89	17.0	23.55	2.36	0.16

[a] High literature BET values are used for all clay minerals except smectite, which is fit to the measured BET surface area (see Section 3.2).
[b] After Mito et al. (2013).

2.4.4. Effective surface area via adjusted ideal geometric surface area

Effective surface areas were estimated from an ideal geometric surface area calculation following the approach used in a previous reactive transport modeling study on the Nagaoka site in Mito et al. (2013). Geometric surface areas were first computed assuming smooth, spherical grains with two uniform grain diameters, 0.004 mm for clay minerals and 0.25 mm for non-clay minerals. The effective surface area, that accounts for surface site reactivity, was then estimated as $3/r$, where r is the grain radius. The grain diameters and scaling approach between specific and effective surface area that were chosen are those used in Mito et al. (2013).

2.5. Disaggregated Nagaoka sediment dissolution rate experiment

A disaggregated sediment dissolution rate experiment was performed to investigate the dissolution rate of the bulk sample with CO_2 saturated fluids under conditions similar to those of the Nagaoka CO_2 injection experiment. The experiment was carried out in a mixed flow-through reactor (Series 4560 Mini Reactor 300 mL, Parr Instruments Company, Moline, IL) at 50 °C and 100 bars pCO_2 partial pressure. The experimental pressure is close to the estimated hydrostatic pressure at the reservoir depth (1093 m) of 107 bars. All parts of the reactors that were in contact with the high temperature aqueous solution were made of Hastelloy C276 or 316 Stainless Steel. Flow rates were controlled by an HPLC pump set to 0.25 ml/min, yielding a residence time within the 300 ml stirred flow-through reactor of 20 h. CO_2 was injected through a supercritical CO_2 pump at a flow rate of 0.1 ml/min to obtain the desired pCO_2 conditions. The experimental system pressure was kept constant with a Jasco BP-2080 adjustable automatic back pressure regulator at 100 bars. The temperature was controlled in the experiments at 50 °C using an automatic temperature controller supplied with the Parr reactor.

One gram of the disaggregated Nagaoka sample was transferred into the reactor for the experiment. CO_2 and saline water (0.1 M NaCl) were first pumped into a mixing tee where they were brought to the experimental temperature. After mixing, the CO_2-saturated solution was pumped into the reactor while maintaining the reactor at the designated pressure and temperature. The solution inside the reactor chamber was constantly mixed by a mechanically driven stirrer placed inside the Parr reactor.

Sample solutions were filtered through a 10 micron Hastelloy filter on the effluent port of the Parr reactor and passed through the automatic back-pressure regulator before dripping into the sample collection vials in a no-oxygen bag continuously flushed with nitrogen. Filtered effluents were collected in clean low-density polyethylene bottles or polypropylene vials. The solutions collected were analyzed for Mg, Fe, Al, K, Ca and Si by a Perkin Elmer DRC-II inductively coupled plasma mass spectroscopy (ICP-MS) after acidification with 2% ultra-pure HNO_3. Due to issues with solution degassing, the pH of the mixed brine and CO_2 solution (the injection solution) and the effluent were not measured. The solution pH of the brine equilibrated with CO_2 was calculated as 3.2 using the equation of state published in Duan and Sun (2003) as implemented in the code CrunchFlow (Steefel et al., 2015b).

2.6. Reactive transport simulation of the experiment

2.6.1. Model description

Continuum reactive transport simulations were carried out to compare against the observations from the rate experiment so as to choose which of the RSA models provided the best description of dissolution behavior. Transient and steady state mineral dissolution rates determined from the flow-through reactor effluent chemistry (see Sections 2.5 and 3.6) were compared with simulations carried out with the multi-component reactive transport model, CrunchFlow (Steefel et al., 2015b). The mineral dissolution rate law used in CrunchFlow is based on transition state theory (or TST) formulation (Aagaard and Helgeson, 1982; Lasaga, 1984; Maher et al., 2009; Steefel et al., 2015b) and is discussed in detail, along with the other pertinent CrunchFlow components, in Appendix C.

Mineral dissolution rate constants, k, (Table 4) were taken from well-stirred reactor dissolution studies of pure minerals available in the literature (Appendix D). As the experimental pH (3.2) and temperature (50 °C) remained constant in this study, the pH and temperature dependences of the rate were folded into the rate constants.

The model is initialized using the mineral distribution (Table 3) determined from the QEMSCAN results (Section 3.1). While specific surface area varies with grain diameter, minerals are initially assumed to have a single grain diameter and corresponding reactive surface area value for each scenario, although this assumption is relaxed in later sections (Section 3.7.3) as needed. As reaction progresses, the mineral surface areas evolve following Eq. (2).

2.6.2. Evaluation of specific and effective surface area approximations

To evaluate the impact of mineral surface area, a total of five model scenarios were run while keeping all other model parameters constant. These scenarios included evaluation of three specific and two effective surface area estimates. For specific surface area scenarios, we considered: (1) low BET and (2) high BET surface areas collected from the literature (Section 2.4.1), and (3) the 2D image perimeter surface area described in Section 2.4.2. For effective surface area scenarios, we considered: (1) the 2D image perimeter surface (Section 2.4.3) area with a scaling factor, and (2) an ideal geometric surface area with scaling factors described in Section 2.4.4. The simulated effluent concentrations of aqueous Ca, Mg, and Si were then compared to the solute concentrations observed in the experiment. Each simulation result was evaluated in terms of how closely these concentrations matched steady-state as well as early time-dependent behavior.

Table 4
Mineral compositions and reaction rate constants used in the modeling.

Mineral	Composition	Log k	Reference(s)
Quartz	SiO_2	−11.48[a]	Brady and Walther (1990)
Plagioclase			
Albite	$NaAlSi_2O_8$	−10.68	Chen and Brantley (1997)
An25	$Ca_{0.61}Na_{0.39}Al_{2.13}Si_2O_8$	−10.16[c]	Gudbrandsson et al. (2014)
Labradorite	$(Ca_{0.62}Na_{0.38})(Al(Al_{0.62}Si_{0.38})Si_2O_8)$	−9.25[b]	McAdam et al. (2008)
Smectite	$(Na_{0.12}Ca_{0.21})(Al_{1.59}Mg_{0.34})(Si_4O_{10})(OH)_2$	−13.11	Amram and Ganor (2005)
K-feldspar	$KAlSi_2O_8$	−10.90[b]	Bevan and Savage (1989)
Pyroxene			
Fe,Mg rich	$Fe_{0.38}Mg_{0.59}Ca_{0.03}SiO_3$	−7.31[c]	Knauss et al. (1993)
Ca,Mg rich	$(Ca_{0.98}Na_{0.02})(Mg_{0.65}Fe_{0.25}Al_{0.1})(Si_{0.96}Al_{0.04})_2O_6$	−9.84[b]	Oelkers and Schott (2001)
Biotite	$K(Ca_{0.06}Mg_{1.02}Fe_{1.92})(AlSi_3)O_{10}(OH)_2$	−11.24[c]	Acker and Bricker (1992)
Amphibole	$Ca_2(Fe_{2.2}Mg_{2.8})Si_8O_{22}(OH)_2$	−10.00[c]	Sverdrup (1990)
Fe Hydroxide	$Fe(OH)_3$	−7.00	–
Chlorite	$(Mg_{2.36}Fe_{2.64})Al(AlSi_3O_{10})(OH)_8$	−10.89[c]	Smith et al. (2013)
Kaolinite	$Al_2Si_2O_5(OH)_4$	−12.07[c]	Carroll and Walther (1990), Ganor et al. (1995)
Pyrite	FeS_2	−7.90	Palandri and Kharaka (2004)
Serpentine	$(Mg_{2.77}Fe_{0.23})Si_2O_5(OH)_4$	−10.65[c]	Daval et al. (2013a)
Ca-phosphate	$Ca_{10}(PO_4)_6(OH)_2$	−7.90	Harouiya et al. (2007)
Calcite	$CaCO_3$	−6.39	Palandri and Kharaka (2004)

[a] Indicates log k is interpolated from rates at temperatures bracketing 50 °C.
[b] Indicates log k extrapolated from data not bracketing 50 °C.
[c] Indicates log k at temperature within range 22–100 °C (on average, 60 °C). Only used when experiments were done at single temperature values and no other sufficient data was available.

3. RESULTS

3.1. 2D SEM imaging

The SEM BSE and segmented images are shown in Fig. 2. The pore and grain boundaries are classified in the thresholded image (Fig. 2C). The QEMSCAN analysis created a map of mineral distribution where each mineral is shown with a different color. While this analysis has the advantage of providing a map of mineral distribution, the SEM BSE images provide higher resolution. Registration of the two images allows the mineral distribution to be added to the high-resolution BSE image. This registered image, including the mineral map, is shown in Fig. 3. In this figure, the *AlSitrap* (see Fig. 3) pixels are unidentified aluminosilicate minerals that did not match any of the other classifications. The *Others* classification refers to minerals that could not be identified by the range of mineral classifications included in, and added to, the QEMSCAN program. As a simplification, the pyroxene and plagioclase groups are displayed as lumped groups in gray or teal, respectively. The plagioclase classification is composed of a range of compositions including intermediate labradorite/An65 (62.9%), albite (30.2%), and An25 (6.9%). The pyroxene classification consists of intermediate phases rich in iron and magnesium (ferrosilite–enstatite) (75.7%) and calcium and magnesium (augite) (20.4%).

Using the registered image, the number of pixels for each mineral was computed and are given as volume percent in Table 3. The most abundant minerals are: quartz (22.6%), plagioclase feldspars (21.4%), smectite (16.9%), K-feldspar (14.62%), and pyroxene (7.2%). Smectite, shown in purple, is the major diagenetic cement in the sample and additionally coats many of the grain surfaces. The mineral abundances in the image analysis agree well with the XRD and XRF analyses, given that all three methods identified the same major mineral phases. As these measurements were performed on different samples from the same larger bulk sample, it is expected that there would be some variation in the mineral distribution. Additionally, QEMSCAN analysis has the potential to localize trace mineral phases that might be missed in bulk analysis due to their small overall mass fraction.

3.2. BET specific surface areas

The BET surface areas for pure minerals collected from existing literature studies are given in Table 3. For some minerals, there is a wide range of existing BET measurements with differences by as much as two orders of magnitude between low and high examples. Variation in BET surface area result from differences in natural alteration, grain size (Acker and Bricker, 1992), and pre-treatment or washing of samples (Zhang et al., 2013), even among

samples obtained from the same source. Taking this observation into account, the range of grain sizes corresponding to the high and low example BET surface areas are also given in Table 3. As there is a wide range of grain sizes in the Nagaoka sample for each mineral (Fig. 3), the example BET surface area values were not limited to a single grain size.

The laboratory measured BET surface area of the Nagaoka sample was determined to be 23.55 m^2/g. This agrees relatively well with the calculated total surface area (17.0 m^2/g) from the high literature BET values of pure minerals. The total surface area from the low literature BET values is one order of magnitude less than both the measured whole sediment BET and high literature values.

3.3. Image perimeter specific surface area

The specific surface areas of minerals in the Nagaoka sample computed from the 2D image perimeter analysis are given in Table 3 and are on the order of 0.1 m^2/g for non-clay minerals. In general, this is within the range of the BET measurements of pure non-clay minerals reported in the literature. As the laboratory measured BET surface area (23.55 m^2/g) for the sample was in closest agreement with the high BET total surface area (17 m^2/g), these values were selected for the clay mineral surface areas with the exception of smectite. The surface area of smectite computed by fitting the total sample surface area to the measured BET surface area is 136.3 m^2/g. This agrees relatively well with the smectite BET surface areas reported in the literature (34–97 m^2/g) (Metz et al., 2005).

3.4. Effective surface area based on scaled image perimeter surface area

Both the image perimeter and BET surface area measurements yield the total surface area and do not account for the distribution of reactive surface sites (effective surface

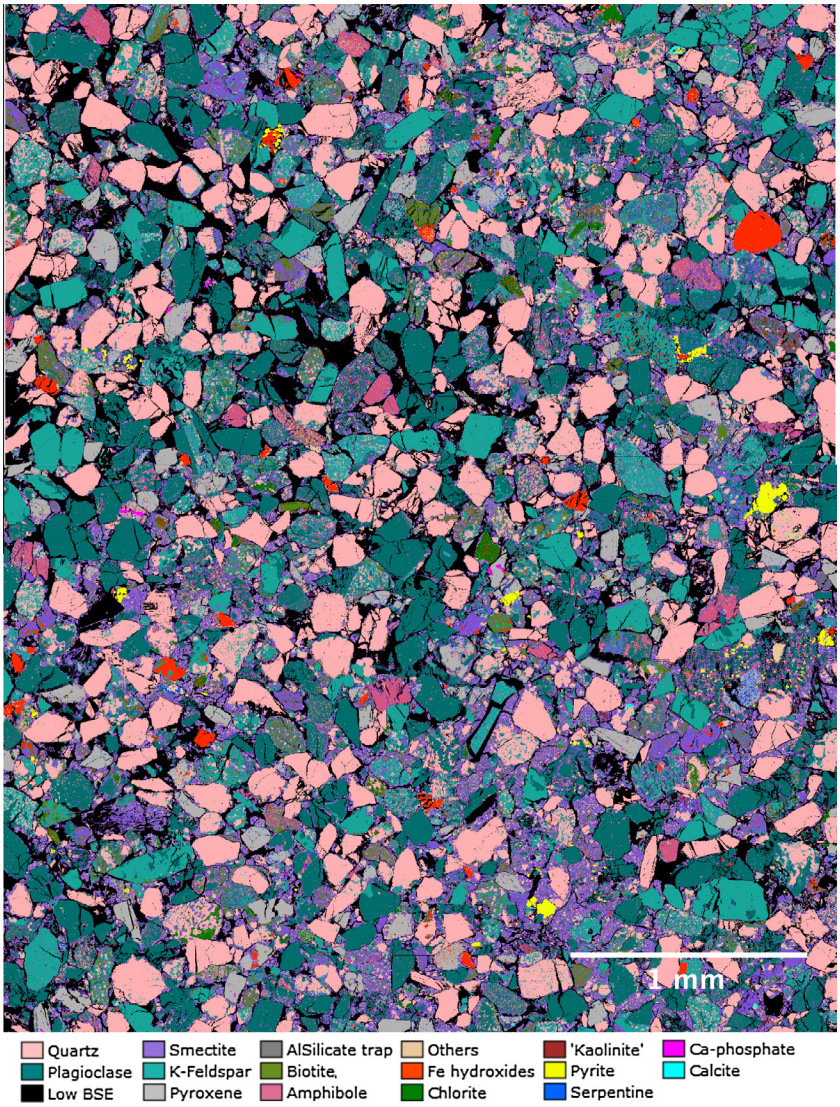

Fig. 3. 2D Registered SEM BSE and QEMSCAN image showing distribution of minerals with variation in pixel color. (For interpretation of the references to color in this figure legend, the reader is referred to the web version of this article.)

area). As discussed above (Section 2.4.3), unconstrained scaling factors are commonly used to account for surface site reactivity. A set of mineral effective surface areas was computed by applying a scaling factor of one order of magnitude to the specific surface area values. The resulting mineral effective surface areas are in Column 6 of Table 3. The effective surface areas for non-clay minerals are in relatively good agreement with the lower range of the pure mineral BET values from the literature. Aside from smectite, the phyllosilicate mineral effective surface areas agree well with the range of BET measurements for the pure minerals. The total estimated surface area in this scenario is 2.36 m^2/g. This is of the same order of magnitude as the lower range of literature BET measurements of pure minerals.

3.5. Effective surface area via adjusted ideal geometric surface area

Mineral effective surface areas computed using the Mito et al. (2013) approach are given in Table 3. Geometric surface areas assumed spherical, smooth grains with distinct grain diameters for clay and non-clay minerals. The resulting effective surface areas for clays (0.64 m^2/g) are two orders of magnitude higher than those for non-clay minerals (0.0091 m^2/g). The total sample effective surface area, computed using the volume fractions determined from the 2D image analysis, is 0.16 m^2/g. For non-clay minerals, the effective surface area values agree relatively well with the image based effective surface areas (Section 3.4). Effective surface area values for clay minerals, however, are two orders of magnitude smaller than those computed from the scaled imaging approach.

3.6. Experimental results

Concentrations of major elements in the effluent of the disaggregated sediment experiment were measured by ICP-MS and are plotted in Fig. 4 as a function of time. A reliable determination of the solution pH was not possible because of issues with solution degassing, so the solution pH in the injection solution and effluent was calculated to be 3.2 at temperature using the routine given by Duan and Sun (2003), as implemented in the code CrunchFlow. After an initial spike, effluent concentrations decline and become fairly constant after 600 h, suggesting steady state conditions were reached. The secondary spike in concentrations observed at approximately 200 h is a result of the pump stopping from 166 to 195 h. The highest observed effluent concentrations are Fe, Si, and K, with steady state concentrations of approximately 10^{-5} mol/kg.

From the data shown in Fig. 4, it is clear that the cation Ca + Mg + K to Si ratio changes significantly over the course of the experiment. This ratio is unusually high in the early stages of the experiment (Fig. 4B), particularly during the pump shutdown (166–195 h), and then decreases systematically through the remainder of the experiment. Based on this ratio, it appears that steady state conditions were not achieved until near the end of the experiment. Also noteworthy is that a large proportion of the Ca, Mg, Fe, and K was released from the sample during the experiment, especially in comparison to the relatively small proportion of silica released (Fig. 4C). The Si data suggest that only about 2–3% of the sample dissolved during the experiment (5% of the sample excluding the relatively inert mineral quartz), whereas almost half of the Ca and 35% of the Fe in the sample was removed. Early in the experiment, the molar ratio of Ca to Si is nearly 1, while Mg is approximately 0.75. The early high concentrations of all of the solutes suggest that a highly reactive phase or phases are controlling the effluent chemistry, while the gradual shift from high to low cation to Si ratios suggests a cation leaching mechanism. While leached layers can form in pure mineral phases (Daval et al., 2013b), this mechanism is unlikely

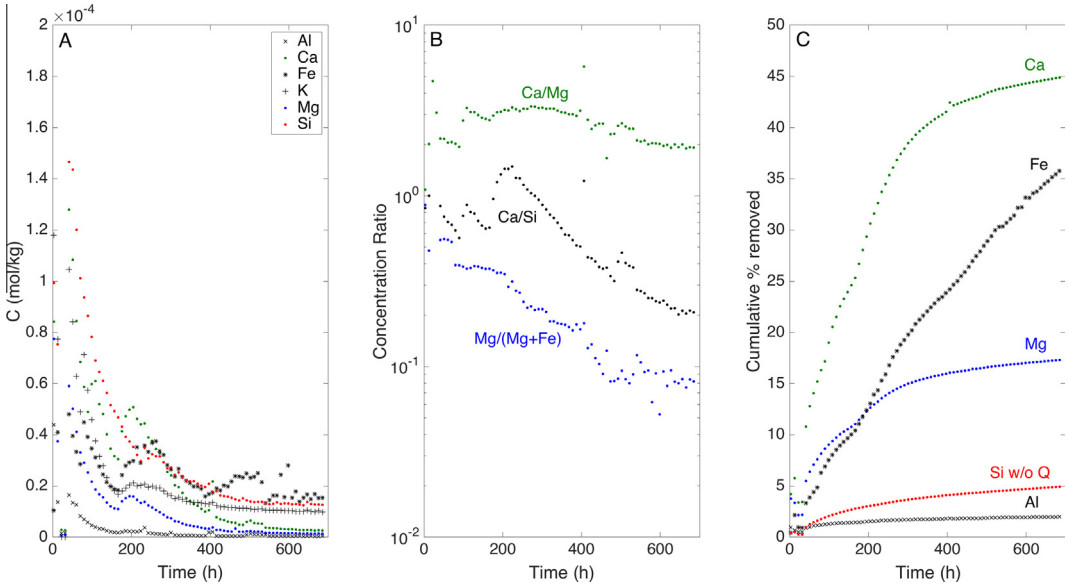

Fig. 4. (A) Effluent concentrations measured from flow-through reactor experiment. (B) Elemental ratios in the effluent through the experiment. (C) Approximate cumulative proportion of the original Ca, Mg, Fe, Si (without quartz) and Al in the sample that was released during the experiment as indicated by comparing the effluent chemistry with the XRF analysis.

to account for the high cation/Si concentrations in the early part of the experiment given the rapid rate of solute release. A more likely explanation for the high cation to Si ratios that gradually decrease with time is a mechanism involving glass dissolution (Marini, 2007; Aradóttir et al., 2013). Aradóttir et al. (2013), for example, observed high cation to Si ratios in an experiment involving dissolution of basaltic glass that extended over 300 pore volumes.

3.7. Reactive transport simulation of the disaggregated sediment experiment

3.7.1. Model parameterization from imaging

The QEMSCAN identified mineral distributions given in Table 3 were used directly in the reactive transport model as initial conditions for the mineralogy. Pyroxene and plagioclase feldspars, although visually displayed as a single color in the QEMSCAN images, were discretized into discrete mineral compositions in the model (Table 3). The corresponding stoichiometry determined from additional SEM EDS analyses of QEMSCAN identified grains is given in Table 4.

3.7.2. Simulation of effluent concentrations using traditional specific and effective surface area estimates

Simulated effluent Ca, Si, and Mg concentrations are shown in Fig. 5 using RSA models based on effective surface areas in shades of orange and specific surface areas in shades of blue. These three elements provide the best description of the dissolution rates of the major phases and thus are the only ones shown against the observations. Solution pH is buffered by the high CO_2 concentrations in the reactor, so it provides essentially no information on the rates and remains constant at a value of 3.2. Fe was also simulated (the entire suite of minerals shown in Table 3 is included), but can only be modeled with the addition of Fe-hydroxide, presumably present as a coating on mineral grains. Since the behavior of the major silicate phases is the focus here, it was decided not to make the dissolution behavior of Fe a focus. In general, there is little difference between the model results using the two effective surface area approximations (orange) and steady state concentrations are reached after approximately 100 h. Simulations that use specific surface area values (blue) are higher than those based on effective surface areas (orange) and show a much larger variation in all cases. The Low BET SSA model runs produce results that agree relatively closely with those based on effective surface areas. At late times, the Image Perimeter SSA results fall between the low and high BET surface area simulated concentrations, but result in higher effluent concentrations for Mg and Si at earlier times (up to ~400 and 150 h, respectively).

In comparison with the experimental effluent concentrations, all of the RSA models runs significantly under-predict the observed peaks in Ca, Mg, and Si concentrations at early times (within the first ~100 h). At later times, steady-state concentrations are not consistently matched, with some simulations over-estimating and some under-estimating steady-state concentrations (Table 5). The Image Perimeter SSA and High BET SA model runs are the closest to approaching time-dependent behavior of Mg and Si, but do not capture the shape and timing of the experimentally-observed peaks. Additionally, they overestimate the observed effluent steady-state concentrations. For Ca, all of the model runs show an approach to steady-state concentrations in the first 100 h, much earlier than the experimental time of ~650 h. For Mg and Si, none of the RSA models reach steady state at times matching the experiment, with some simulations reaching steady-state at earlier times (Low BET SA, scaled GSA, scaled Image

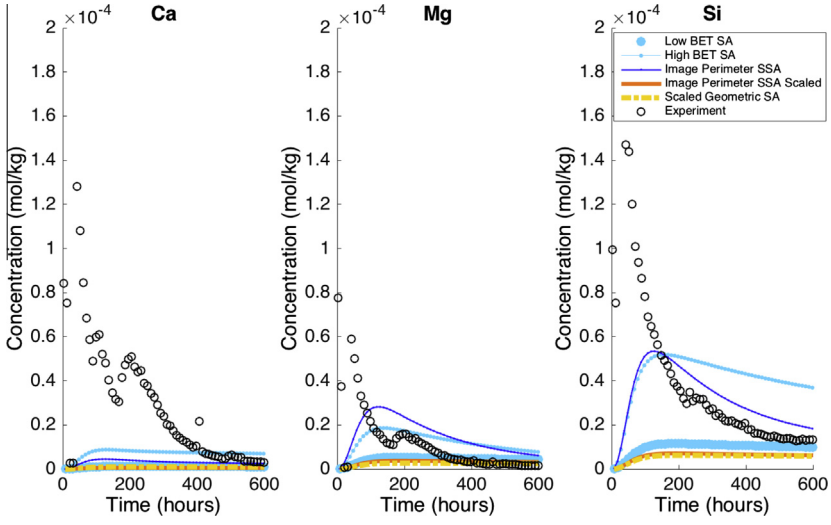

Fig. 5. Experimental (open circles) and simulated effluent ion concentrations from single grain size model, with blue and orange lines corresponding to specific and effective surface areas respectively. (For interpretation of the references to color in this figure legend, the reader is referred to the web version of this article.)

Table 5
Simulated steady-state effluent concentrations from single grain size models using specific and effective surface area values (Table 3).

Species	Experimental (mol/kg)	Specific surface area			Effective surface area	
		Low BET (mol/kg)	High BET (mol/kg)	Image perimeter (mol/kg)	Image perimeter Scaled (mol/kg)	Scaled ideal geometric (mol/kg)
Ca	2.63E−6	1.12E−6	6.90E−6	2.56E−6	5.12E−7	9.55E−7
Mg	1.37E−6	4.20E−6	7.08E−6	5.39E−6	3.17E−6	2.53E−6
Si	1.26E−5	9.80E−6	3.56E−5	1.71E−5	6.14E−6	5.85E−6

Perimeter) and some at later times (High BET SA, Image Perimeter SSA). The mismatch of the model and experimental results suggests that either the model surface area values are incorrect, or additional processes are occurring that are not included in the model. Both of these possible explanations are investigated in the following section.

3.7.3. Alternative reactive surface area formulations

One possible explanation for the poor fit of the simulations to the experimental data is that the reactive surface area values that were used are not correct. Given that simulations using specific and effective surface areas were unable to adequately match the experimental effluent concentrations, additional adjustments in reactive surface areas were made to improve the fits. Keeping the total volume fractions of each mineral constant, surface areas in the model were tuned to try to match both the experimental steady-state and time-dependent concentrations of Ca, Mg, and Si, capturing peak timing and tail trend without sacrificing the steady-state fit (results not shown). As the secondary peak is an experimental artifact resulting from pump stoppage, it was not included in the model or model evaluation. No combination of surface area values yielded model concentrations that matched early peak timing and steady-state concentrations satisfactorily. The largest mismatch was in the simulation of the observed early-time spikes in effluent ion concentrations. The conclusion is that using single values for the RSA of the minerals listed in Table 3, it is impossible to capture both the early time peaks and the steady state effluent concentrations. It should be noted that supersaturation of mineral phases was not observed in these, or any of the following, simulations.

These early-time peaks suggest two interrelated phenomena are likely occurring: (1) dissolution of fine-grained particles with potentially both higher specific surface area and higher reactivity and (2) dissolution of a highly reactive glass phase, that was detected based on SEM analysis. To test the possibility of these processes, trial runs were carried out incorporating a range of grain sizes from 25 nm up to 280 microns for the most reactive phases based on image mapping. This was followed by further refinement of the reactivity and composition of the amorphous glass phase to the extent that this was necessary to match the experimental results.

Simulations incorporating grain size distributions. Grain size distributions for pyroxene and plagioclase (based on image mapping) were incorporated into the model as discrete size fractions. The areas of plagioclase and pyroxene grains were determined by counting the number of pixels in pyroxene and plagioclase mineral grains in the registered 2D image (Fig. 3). Assuming spherical grains, the diameter of the corresponding grains was computed and a 2D bias correction factor of $\pi/4$ was applied. The grain size distributions were then separated into discrete 20 μm diameter bins (Tables 6 and 7). The total volume of plagioclase and pyroxene minerals was computed and used to determine the volume fractions for each grain size bin. These fractions were then allocated to individual pyroxene or plagioclase mineral phases (Table 3). The weighted average grain diameter was computed for each bin and used to represent the bin, with the exception of the smallest grain size bin. This bin was sub-divided into four grain sizes that are assumed to be 0.025, 0.1, 0.5 and 5 μm, as limitations in the QEMSCAN image spatial resolution did not allow for quantification of grain size distributions below 5 μm.

The following relationship between BET specific surface area and grain size was used to compute the specific surface areas for each bin:

$$\mathrm{GSA} = \frac{A_s}{m} = \frac{4\pi r^2}{4/3\pi r^3 \rho} = \frac{3}{r\rho} \tag{3}$$

$$\mathrm{SSA} = \mathrm{GSA} * \mathrm{RF} = \frac{3}{r\rho} * \mathrm{RF} \tag{4}$$

where A_s is the total surface area of the mineral grain, m is the particle mass, r is the grain radius, and ρ is the mineral density. The SSA (specific surface area) is the product of geometric surface area (GSA) and a grain surface roughness factor (RF). The RF was determined to be 4.3 for pyroxene based on a fit to experimental BET data from the literature for a variety of pyroxene minerals (Fig. 6). The RF for feldspar, from existing literature, ranges from one to twenty (Hodson, 1999).

Grain size distribution Run 1: multiple grain sizes for plagioclase and pyroxene minerals with RF = 4.3. In this scenario, a RF of 4.3 was used to compute the specific surface areas for pyroxene and feldspar minerals (Eqs. (1) and (2)). The corresponding grain diameters and specific surface areas are given in Tables 6 and 7 for pyroxene and plagioclase. With the exception of the incorporation of multiple grain sizes for the plagioclase and pyroxene phases, all other model parameters were the same as the runs described above (Section 3.7.2) using the single grain size high BET surface area values for the other minerals (Table 3).

Table 6
Grain sizes and corresponding calculated surface areas for pyroxene minerals used in the grain size distribution (GSD) model. Volume fractions and average grain diameters computed from image analysis with the exception of the smallest bin size that was assigned representative grain diameters at equal fractions (25% each of the smallest bin mapped from the image analysis), indicated in the table by *.

Grain size (μm)	Weighted average diameter (μm)	Pyroxene – Fe rich		Pyroxene – Ca rich	
		Volume % of total pyroxene	Surface area (m^2/g)	Volume % of total pyroxene	Surface area (m^2/g)
1–20	0.025*	0.0071	271.58	0.0022	312.73
1–20	0.1*	0.0071	67.89	0.0022	78.18
1–20	0.5*	0.0071	13.58	0.0022	15.64
1–20	5*	0.0071	1.36	0.0022	1.56
20–40	23.44	0.74	0.29	0.23	0.33
40–60	44.77	3.90	0.15	1.23	0.17
60–80	67.27	7.72	0.10	2.43	0.12
80–100	90.30	8.97	0.075	2.83	0.087
100–120	108.59	14.21	0.063	4.47	0.072
120–140	127.31	27.01	0.053	8.51	0.061
140–160	142.78	5.85	0.048	1.84	0.055
160–180	165.06	4.51	0.041	1.42	0.047

Table 7
Volume fractions and corresponding calculated surface areas for plagioclase minerals used in grain size distribution (GSD) model. Four representative grain diameters were selected to further discretize the smallest grain size bin (indicated by *), as image resolution was not good enough to resolve these below about 5 μm.

Grain size (μm)	Weighted average diameter (μm)	Albite		An25		Labradorite	
		Volume % of total plagioclase	Surface area (m^2/g)	Volume % of total plagioclase	Surface area (m^2/g)	Volume % of total plagioclase	Surface area (m^2/g)
1–20	0.025*	0.00070	393.89	0.00016	375.27	0.0015	379.41
1–20	0.1*	0.00070	98.47	0.00016	93.82	0.0015	94.85
1–20	0.5*	0.00070	19.69	0.00016	18.76	0.0015	18.97
1–20	5*	0.00070	1.97	0.00016	1.88	0.0015	1.89
20–40	23.38	0.32	0.42	0.07	0.40	0.66	0.41
40–60	43.02	1.26	0.23	0.29	0.22	2.63	0.22
60–80	66.99	1.79	0.15	0.41	0.14	3.72	0.14
80–100	90.22	1.67	0.11	0.38	0.10	3.47	0.11
100–120	108.94	2.04	0.091	0.47	0.086	4.24	0.087
120–140	131.07	2.19	0.075	0.51	0.072	4.57	0.072
140–160	150.12	2.53	0.066	0.58	0.062	5.27	0.063
160–180	166.74	3.47	0.059	0.80	0.056	7.22	0.057
180–200	190.33	4.13	0.052	0.95	0.049	8.60	0.049
200–220	212.11	1.42	0.046	0.33	0.044	2.97	0.045
220–240	227.50	2.64	0.043	0.61	0.041	5.49	0.042
240–260	247.05	3.38	0.039	0.78	0.038	7.04	0.038
260–280	274.33	3.08	0.036	0.71	0.034	6.42	0.034

Simulations of effluent ion concentrations from this scenario are shown as dashed bright red lines ('RF = 4.3; No glass') in Fig. 7. The overall timing and shapes of the early peaks in these model simulations for Ca, Mg, and Si are an improvement over any of the matches achieved with the five single value surface area estimates (Fig. 5) described above. However, the observed experimental peak heights for all ions are still under-predicted by as much as 1/6–1/3 of the observed values, indicating the reactivity at early times is not adequately captured. The significant improvement in the early-time peaks in comparison to prior single-grain size models, however, suggests the presence of fine-grained materials.

Grain size distribution Run 2: multiple grain sizes for plagioclase and pyroxene minerals with RF = 10. One possibility for the observed model misfit might be the choice of too low a surface roughness factor. A larger roughness factor would increase specific surface area and thus reactivity. In this scenario, the RF is increased to a value of 10 (a commonly used value in the literature) from the value of 4.3 that was determined by a fit of the data shown in Fig. 6. All other model parameters and grain sizes were identical to the previous grain size model described above.

The simulation results shown in Fig. 7 as dark red dashed lines ('RF = 10; No glass') still fail to match satisfactorily the experimental results. While the predicted peak

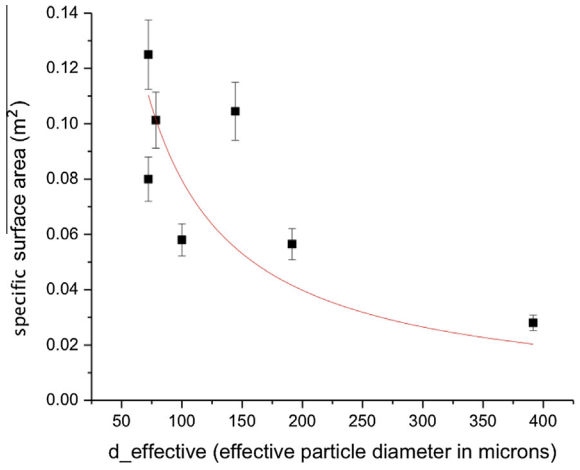

Fig. 6. Literature values of pyroxene BET surface area (Knauss et al., 1993; Oelkers and Schott, 2001; Golubev et al., 2005; Dixit and Carroll, 2007; Daval et al., 2010; Stockmann et al., 2013) and their corresponding effective grain sizes where effective particle diameter (de) = (dmax–dmin)/ln(dmax/dmin) (Tester et al., 1994). The roughness factor was determined as 4.3 from a best-fit line of Eq. (2) with standard error of 0.54.

heights are higher than the run with a RF of 4.3, and thus closer to the experimental peak heights, they still significantly under-predict the experimental values. Additionally, the use of an RF of 10 results in a worse match of steady-state simulation concentrations compared to a roughness factor of 4.3 (Table 8).

Simulations incorporating glass. A significant occurrence of amorphous or poorly crystalline material was observed in the Nagaoka sample based on the 2D SEM imaging (Fig. 3). In the QEMSCAN analysis, the bulk of this material, which in some cases has the appearance of cement, was initially labeled as smectite. The sample, however, also contains an amorphous phase (Section 2.2) that is difficult to distinguish from the smectite based on the QEMSCAN analysis due to its compositional similarity. The XRD analysis (Section 2.2) identified 8.5% of the sediment as amorphous material in the sample. This suggests as much as 50% of the phase mapped as smectite (17% of the sediment, Table 3) may in fact be glass or other amorphous or poorly crystalline material. Some grains show evidence of bubbles, a strong suggestion that they represent a discrete glass phase.

In this modeling scenario, the major fine-grained phase was separated into smectite and glass, with the percentage of each treated as adjustable so as to provide the optimal fit of the effluent chemistry data. We have no real basis for quantifying the exact fraction of each of these with the characterization approaches we have access to, so we rely on the modeling to estimate this, even if this introduces another variable into the simulation. In each of these runs, the total pool of smectite + glass corresponds to what is given in Table 3. The mass of glass versus smectite included

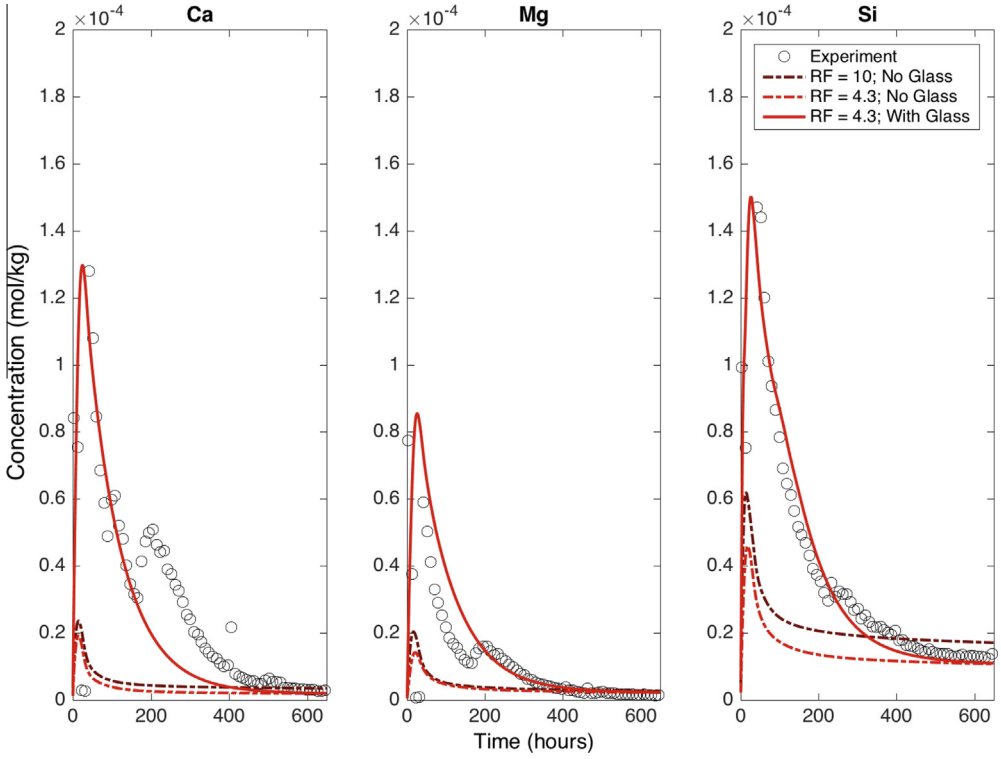

Fig. 7. Observed (black circles) and model predicted (red lines) effluent concentrations incorporating grain size distributions for plagioclase and pyroxene minerals, with and without inclusion of glass phase. (For interpretation of the references to color in this figure legend, the reader is referred to the web version of this article.)

Table 8
Comparison of experimental and simulated steady-state values from both grain size distribution runs and glass run (Fig. 7).

Species	Experimental (mol/kg)	RF = 4.3; No Glass (mol/kg)	RF = 10; No Glass (mol/kg)	RF = 4.3; With Glass (mol/kg)
Ca	2.63E−6	1.91E−6	3.45E−6	2.02E−6
Mg	1.37E−6	2.20E−6	2.75E−6	2.28E−6
Si	1.26E−5	1.08E−5	1.71E−5	1.10E−5

in the simulation primarily influenced how long-lived the early concentration peaks were.

The composition of this phase was determined by adjusting the composition until a satisfactory model fit with the early peak effluent chemistry was achieved. This resulted in the following stoichiometry for glass dissolution, with the negative stoichiometric coefficient for H^+ indicating it is consumed in the reaction:

$$-4.32'H^{+\prime}\ 0.98'Ca^{++\prime}\ 0.18'Al^{+++\prime}\ 1.6000'SiO_2(aq)'\ 2.16'H_2O'\ 0.02'Na^{+\prime}\ 0.25'Fe^{++\prime}\ 0.65'Mg^{++\prime}, \quad (5)$$

A stoichiometry that is close in composition to what would be produced by the dissolution of a silica-poor clinopyroxene. This silica-poor and cation rich "fictive phase" does not correspond to the bulk composition of basaltic glass, however, since the cation to silica ratios are too high. It does have some similarity to the effluent chemistry associated with leaching of basaltic glass considered by Marini (2007), who modeled the cations and silica-rich portions of the glass as separate phases. The high early cation to silica ratio presumably reflects the formation of a leached layer in the glass. A more rigorous way to model this effect would be to incorporate the leached layer formation, although this would involve tracking the progression of the leaching front in the glass to capture the increasing diffusion length scale (Steefel et al., 2015a). Aradóttir et al. (2013) considered a diffusion controlled system in their modeling study of basaltic glass dissolution, but they treated the diffusion length as fixed, which precluded the possibility of simulating a time-dependent cation to silica ratio.

This phase was fit based on the initial peak and steady state concentrations with a log k rate constant value of −7.5 and surface area of 1 m^2/g, since both the rate constant and the RSA could not be independently determined. However, this is about one order of magnitude slower than the rate for basaltic glass dissolution used by Aradóttir et al. (2013), which they based on the study of Oelkers and Gislason (2001). It should be noted that regardless of the rate of the basaltic glass leaching and the volume of basaltic glass used in the simulations, a phase close to the stoichiometry given in Eq. (3) above is required to match the effluent chemistry.

Glass Run 1: multiple grain sizes for plagioclase and pyroxene minerals with RF = 4.3 and glass. This model run uses the same parameters as that described in '*Grain size distribution Run 1*' with the addition of the amorphous glass or cement phase of approximately CPX composition. The percentage of the glass phase was 10% of the total cement phase (smectite in Table 3) and was determined by tuning the fractions of smectite and glass up to a maximum of 50% until a satisfactory fit was observed in the early peak heights and durations for Ca, Mg, and Si. As the glass fraction was changed, the corresponding surface area of smectite was adjusted such that their total contribution to the BET surface area remained constant.

Simulated effluent ion concentrations are shown as a solid red line in Fig. 7 ('SRF = 4.3, With Glass'). Compared to the other simulations, this scenario shows a substantially improved fit with model peak heights and shapes as well as durations that match experimental peaks very closely. In addition, steady-state Ca, Mg, and Si concentrations are also matched closely (Table 8).

Glass Run 2: evaluation of effective and specific surface areas with multiple grain sizes for plagioclase and pyroxene minerals (RF = 4.3) and glass. In the first glass run, the need to include the highly reactive amorphous phase was demonstrated by the significant improvement in the model fit, particularly at early times. The first run used the single grain size high BET surface area values for all non-pyroxene and plagioclase minerals. In this second model run, the entire suite of effective and specific surface areas (Table 3) is evaluated. The parameters are the same as in the first run, except in the Image Perimeter SSA Scaled scenario in which the surface area of the amorphous phase was computed as 0.1 m^2/g after the scaling factor (Section 2.4.3) was applied.

The resulting simulated effluent concentrations are shown in Fig. 8. As in the single-grain models (Fig. 5), the simulations from models using effective surface area values are shown in orange and specific surface area values in blue. The simulations using specific surface area values agree relatively well with each other and the experimentally observed concentrations. The Scaled Ideal Geometric surface area over-estimates the initial Si peak, but is otherwise close to the specific surface area simulations. Simulated concentrations from the Scaled Image Perimeter run underestimate the initial peaks and overestimate the steady-state concentrations (Table 9) in all cases. The large observed differences from the other simulations are a result of the lower glass phase surface area in this run, 0.1 m^2/g vs. 1 m^2/g. The lower surface area reduces the reactivity of the phase, decreasing the initial peak height and increasing the time for the phase to dissolve. In the other simulation results shown here, the glass phase is depleted and steady-state is reached within the simulation time. In the Scaled Image Perimeter simulation, however, the glass phase is still dissolving after 600 h and steady-state conditions are not reached.

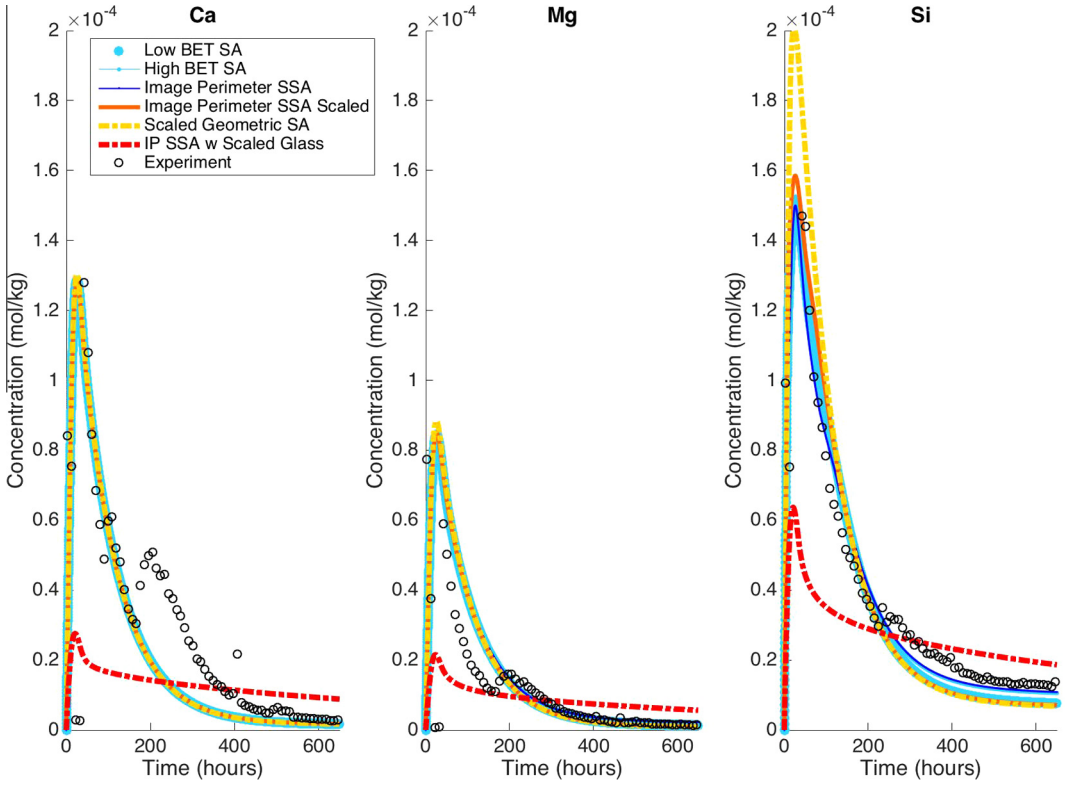

Fig. 8. Simulated effluent concentrations with glass phase and grain size distribution for pyroxene and plagioclase minerals. All other minerals are modeled using the single grain size surface area estimates from Table 3. The glass phase surface area is 1.0 m^2/g in all runs except "IP SSA w Scaled Glass" where the glass phase surface area is 0.1 m^2/g.

Table 9
Simulated steady-state effluent concentrations for models including grain size distributions for pyroxene and plagioclase minerals and glass phase.

Species	Experimental (mol/kg)	Specific surface area			Effective surface area	
		Low BET (mol/kg)	High BET (mol/kg)	Image perimeter (mol/kg)	Image perimeter scaled (mol/kg)	Scaled ideal geometric (mol/kg)
Ca	2.63E−6	1.65E−6	1.97E−6	1.95E−6	8.51E−6	2.28E−6
Mg	1.37E−6	1.19E−6	2.23E−6	2.21E−6	5.48E−6	1.70E−6
Si	1.26E−5	7.51E−6	1.09E−5	1.07E−5	1.80E−5	8.95E−6

4. DISCUSSION

4.1. Comparison of mineral surface areas

There is up to three orders of magnitude variation in the estimation of mineral surface areas (Table 3) depending on the approximation method used. Some of this variation, including between specific and effective surface area, is expected as order of magnitude scaling factors are applied to compute the effective surface areas (Bourg et al., 2015). In addition, there are one or more orders of magnitude variation among specific or effective surface area values themselves. With regard to specific surface areas, the estimates from the imaging method that account for sample specific features generally fall within the range of BET surface areas of pure minerals from the literature. However, given that there is as much as two orders of magnitude between the high and low literature BET surface areas, this may not serve as an effective guideline for which sample-specific surface areas to use in modeling. Variations in single mineral surface areas translate into orders of magnitude variation in the total sample surface area values (bottom row of Table 3). Total surface areas span two orders of magnitude between effective and specific surface areas and one order of magnitude among specific or effective surface area estimates.

4.2. Evaluation of model-experiment match

The model results using the suite of reactive surface area models span just over one order of magnitude for steady-state concentrations and initial concentration peaks

(Fig. 5). This is similar to the variation observed among mineral surface area values (Section 4.1). This correlation is expected given that the mineral reaction rate is directly proportional to mineral surface area (Appendix C). Thus, inaccuracies in mineral reactive surface area directly impact the ability to match effluent concentrations.

Simulation of effluent steady state concentrations using the two estimates of mineral effective surface area produce results that agree relatively well with each other. This may be surprising as the estimate of effective surface areas made following the adjusted geometric approach (Section 2.4.4) do not account for sample-specific characteristics such as grain size and additionally assume uniform effective surface areas for all clay minerals and non-clay minerals, respectively. In spite of their agreement with each other, the simulation results using the effective surface area estimates were unable to match experimental observations of effluent concentrations, particularly at early times where no initial peaks in effluent concentrations were simulated. In contrast, the model simulations using the specific surface areas result in a larger range of effluent concentrations. While some of the simulations do show an early peak in effluent concentrations, all of the simulations fail to capture the peak height and timing.

Given that the Nagaoka formation is a volcanogenic sandstone composed of many reactive minerals, including clays, plagioclase, pyroxene, and glass, it is not surprising that a relatively complex model is required to simulate the dissolution rate of the sedimentary rock. Additional necessary model complexities include the incorporation of multiple grain sizes of some of the most reactive minerals as well as a highly reactive glass phase that displays early cation leaching. The addition of smaller-grain sizes did produce early solute concentration peaks that were not generated by the single grain size simulations, because these finer grained materials have a high surface area and thus higher reactivity than the coarse grained materials. The presence of a range of grain sizes was evident from the 2D SEM imaging analysis.

The leaching of the glass phase has been noted in many studies of basaltic glass dissolution resulting in high cation to silica ratios that gradually decrease with time as the diffusion length scale in the leached layer increases (Aradóttir et al., 2013). Simulations with the glass phase included were able to successfully reproduce the early time peaks in effluent concentrations. The addition of the glass phase is a key component to reproducing the early peaks in concentrations, as also evident from simulations run with the amorphous phase and without the grain size distributions for pyroxene and plagioclase minerals (Appendix E).

For sediment in which the pore structure remains intact, the dissolution of glass-cement that acts to aggregate sections of the solid will likely not cause disaggregation in the same fashion as we observed in this dissolution experiment. We expect that in the case of a core, glass dissolution will impact porosity and permeability as well as influence the number and distribution of available reactive sites on minerals that persist longer than the glass phase. The difference in dissolution kinetics among minerals present in the rock and their spatial distribution will have to be taken into account when trying to determine the evolution of reactive surface areas in a porous solid.

The selection of a roughness factor directly influences the ability to match initial peak heights as well as the steady-state concentrations. While the roughness factor used here was determined from a fit of BET specific surface areas from existing literature on pyroxenes, natural variation is expected based on the extent of weathering and reaction that has previously occurred. Modification in the surface roughness alone, however, was not sufficient enough to simulate the observed effluent data.

With the addition of the glass phase displaying cation leaching and a grain size distribution for the most reactive minerals, the Image Perimeter specific surface areas followed by the BET surface areas provided the best fits of the model results with the experimental effluent data. These surface areas provide a measure of specific surface area that account for surface roughness. Effectively, these surface areas quantify the physical surface area that is in contact with the reacting fluid, but do not capture the density of reactive sites on the individual mineral surfaces.

4.3. Results in a GCS context

One notable aspect of the conducted experiment was the rapid observed release of cations (particularly Ca & Mg) during the flow-through experiment, despite the relatively low temperature. While, as demonstrated, this rate can be fully explained by the reactive mineral assemblage, glass phase, and proper treatment of surface area, the resulting aqueous concentrations are sufficient to lead to CO_2 mineralization in relatively short (decadal) time frames. Our experimental results are consistent with field geochemical measurements from the Nagaoka pilot, in particular the fluid samples analyzed in Mito et al. (2008) which revealed both elevated cation concentrations (Ca, Mg, & Fe) as well as elevated Ca/Si and Mg/Si ratios after CO_2 injection. These samples, obtained using a cased hole dynamics tester (CHDT) tool from observation well OB-2, provide evidence that the proposed glass dissolution mechanism may have field relevance at the site. More generally, our results suggest that improved mineral trapping rates at GCS sites could be achieved by screening reservoirs for reactivity as well as reactive surface area and targeting relatively young volcanogenic sandstones as advocated by Zhang et al. (2013).

4.4. Implications and recommendations

Understanding the potential complexities and heterogeneities of the reacting sample is critical to accurately simulating mineral reaction rates. In particular, a thorough understanding of reactive minerals/phases and their accessibility to reactive fluids is necessary. In this effort, this includes not only accounting for the fine-grained reactive minerals, but additionally the presence of a highly reactive glass phase within which the formation of a leached layer resulted in preferential release of cations relative to silica. The 2D SEM imaging provides invaluable insight on the grain size distributions of minerals and the presence of

coated and cemented grains. With these complexities accounted for, *specific surface areas* are able to successfully predict the reactivity of the complex, multi-mineralic Nagaoka sediment. This is a key finding in that corrections for the reactivity of surface sites may not be necessary as was observed here. In this scenario, the closest match to the observed experimental concentrations was obtained using image-based specific surface area values. However, it is also of note that simulations using literature obtained values of specific surface areas are in relatively good agreement with the image-based simulation results in comparison with the effective surface area simulations. This suggests that literature obtained specific surface areas may provide a reasonable approximation of reactive surface areas in disaggregated scenarios. This, however, may still require accounting for grain size distributions and sample specific phenomena, such as glass dissolution, as in the simulations in this investigation.

ACKNOWLEDGEMENTS

This work was supported as part of the Center for Nanoscale Control of Geologic CO_2 (NCGC), an Energy Frontier Research Center funded by the U.S. Department of Energy, Office of Science, Basic Energy Sciences under Award # DE-AC02-05CH11231. Rock sample collection at the Nagaoka pilot CO_2 injection site was financed by Ministry of Economy, Trade and Industry (METI) under the contract of "Research and Development of Underground Storage for Carbon Dioxide".

APPENDIX A. SUPPLEMENTARY DATA

Supplementary data associated with this article can be found, in the online version, at http://dx.doi.org/10.1016/j.gca.2016.05.040.

REFERENCES

Aagaard P. and Helgeson H. C. (1982) Thermodynamic and kinetic constraints on reaction rates among minerals and aqueous solutions. I. Theoretical considerations. *Am. J. Sci.* **282**, 237–285.

Acker J. G. and Bricker O. P. (1992) The influence of pH on biotite dissolution and alteration kinetics at low temperature. *Geochim. Cosmochim. Acta* **56**, 3073–3092.

Alemu B. L., Aagaard P., Munz I. A. and Skurtveit E. (2011) Caprock interaction with CO_2: a laboratory study of reactivity of shale with supercritical CO_2 and brine. *Appl. Geochem.* **26**, 1975–1989.

Amram K. and Ganor J. (2005) The combined effect of pH and temperature on smectite dissolution rate under acidic conditions. *Geochim. Cosmochim. Acta* **69**, 2535–2546.

Aradóttir E. S. P., Sigfússon B., Sonnenthal E. L., Björnsson G. and Jónsson H. (2013) Dynamics of basaltic glass dissolution – capturing microscopic effects in continuum scale models. *Geochim. Cosmochim. Acta* **121**, 311–327.

Arganda-Carreras I., Sorzano C. O. S., Kybic J. and Ortiz-de-Solorzano C. (2008) BUnwarpJ: consistent and elastic registration in ImageJ. Methods and applications. In *Presented at the Second ImageJ User & Developer Conference*.

Beckingham L. E., Peters C. A., Um W., Jones K. W. and Lindquist W. B. (2013) 2D and 3D imaging resolution trade-offs in quantifying pore throats for prediction of permeability. *Adv. Water Resour.* **62**, 1–12.

Bevan J. and Savage D. (1989) The effect of organic acids on the dissolution of K-feldspar under conditions relevant to burial diagenesis. *Mineral. Mag.* **53**, 415–425.

Black J. R. and Haese R. R. (2014) Chlorite dissolution rates under CO_2 saturated conditions from 50 to 120°C and 120 to 200 bar CO_2. *Geochim. Cosmochim. Ac* **125**, 225–240.

Black J. R., Carroll S. A. and Haese R. R. (2015) Rates of mineral dissolution under CO_2 storage conditions. *Chem. Geol.* **399**, 134–144.

Bolourinejad P., Shoeibi Omrani P. and Herber R. (2014) Effect of reactive surface area of minerals on mineralization and carbon dioxide trapping in a depleted gas reservoir. *Int. J. Greenhouse Gas Control* **21**, 11–22.

Bourg I. C., Beckingham L. E. and DePaolo D. J. (2015) The nanoscale basis of CO_2 trapping for geologic storage. *Environ. Sci. Technol.* **49**, 10265–10284.

Bracco J. N., Stack A. G. and Steefel C. I. (2013) Upscaling calcite growth rates from the mesoscale to the macroscale. *Environ. Sci. Technol.* **47**, 7555–7562.

Brady P. V. and Walther J. V. (1990) Kinetics of quartz dissolution at low temperatures. *Chem. Geol.* **82**, 253–264.

Brunauer S., Emmett P. H. and Teller E. (1938) Adsorption of gases in multimolecular layers. *J. Am. Chem. Soc.* **60**, 309–319.

Carroll S. A. and Walther J. V. (1990) Kaolinite dissolution at 25, 60, and 80 C. *Am. J. Sci.* **290**, 797–810.

Casey W. H., Westrich H. R. and Holdren G. R. (1991) Dissolution rates of plagioclase at pH = 2 and 3. *Am. Mineral.* **76**, 211–217.

Chen Y. and Brantley S. L. (1997) Temperature- and pH-dependence of albite dissolution rate at acid pH. *Chem. Geol.* **135**, 275–290.

Chiyonobu S., Nakajima T., Zhang Y., Tsuji T. and Xue Z. (2013) Effect of reservoir heterogeneity of Haizume Formation, Nagaoka Pilot Site, based on high-resolution sedimentological analysis. *Energy Procedia* **37**, 3546–3553.

Crandell L. E., Peters C. A., Um W., Jones K. W. and Lindquist W. B. (2012) Changes in the pore network structure of Hanford sediment after reaction with caustic tank wastes. *J. Contam. Hydrol.* **131**, 89–99.

Daval D., Hellmann R., Corvisier J., Tisserand D., Martinez I. and Guyot F. (2010) Dissolution kinetics of diopside as a function of solution saturation state: macroscopic measurements and implications for modeling of geological storage of CO_2. *Geochim. Cosmochim. Acta* **74**, 2615–2633.

Daval D., Hellmann R., Martinez I., Gangloff S. and Guyot F. (2013a) Lizardite serpentine dissolution kinetics as a function of pH and temperature, including effects of elevated pCO_2. *Chem. Geol.* **351**, 245–256.

Daval D., Hellmann R., Saldi G. D., Wirth R. and Knauss K. G. (2013b) Linking nm-scale measurements of the anisotropy of silicate surface reactivity to macroscopic dissolution rate laws: new insights based on diopside. *Geochim. Cosmochim. Acta* **107**, 121–134.

Descostes M., Vitorge P. and Beaucaire C. (2004) Pyrite dissolution in acidic media. *Geochim. Cosmochim. Acta* **68**, 4559–4569.

Devidal J.-L., Schott J. and Dandurand J.-L. (1997) An experimental study of kaolinite dissolution and precipitation kinetics as a function of chemical affinity and solution composition at 150 C, 40 bars, and pH 2, 6.8, and 7.8. *Geochim. Cosmochim. Acta* **61**, 5165–5186.

Dixit S. and Carroll S. A. (2007) Effect of solution saturation state and temperature on diopside dissolution. *Geochem. Trans.* **8**, 3–14.

Domenech C., de Pablo J. and Ayora C. (2002) Oxidative dissolution of pyritic sludge from the Aznalcóllar mine (SW Spain). *Chem. Geol.* **190**, 339–353.

Duan Z. and Sun R. (2003) An improved model calculating CO_2 solubility in pure water and aqueous NaCl solutions from 273 to 533 K and from 0 to 2000 bar. *Chem. Geol.* **193**(3), 257–271.

Frogner P. and Schweda P. (1998) Hornblende dissolution kinetics at 25 C. *Chem. Geol.* **151**, 169–179.

Ganor J., Mogollon J. L. and Lasaga A. C. (1995) The effect of pH on kaolinite dissolution rates and on activation energy. *Geochim. Cosmochim. Acta* **59**, 1037–1052.

Gaus I. (2010) Role and impact of CO_2–rock interactions during CO_2 storage in sedimentary rocks. *Int. J. Greenhouse Gas Control* **4**, 73–89.

Gaus I., Audigane P., André L., Lions J., Jacquemet N., Durst P., Czernichowski-Lauriol I. and Azaroual M. (2008) Geochemical and solute transport modelling for CO_2 storage, what to expect from it? *Int. J. Greenhouse Gas Control* **2**, 605–625.

Golubev S. V., Pokrovsky O. S. and Schott J. (2005) Experimental determination of the effect of dissolved CO_2 on the dissolution kinetics of Mg and Ca silicates at 25 C. *Chem. Geol.* **217**, 227–238.

Gualtieri A. F. (2000) Accuracy of XRPD QPA using the combined Rietveld – RIR method. *J. Appl. Crystallogr.* **33**, 267–278.

Gudbrandsson S., Wolff-Boenisch D., Gislason S. R. and Oelkers E. H. (2014) Experimental determination of plagioclase dissolution rates as a function of its composition and pH at 22 °C. *Geochim. Cosmochim. Acta* **139**, 154–172.

Gunter W. D., Perkins E. H. and Hutcheon I. (2000) Aquifer disposal of acid gases: modelling of water–rock reactions for trapping of acid wastes. *Appl. Geochem.* **15**, 1085–1095.

Harouiya N., Chaïrat C., Köhler S. J., Gout R. and Oelkers E. H. (2007) The dissolution kinetics and apparent solubility of natural apatite in closed reactors at temperatures from 5 to 50 °C and pH from 1 to 6. *Chem. Geol.* **244**, 554–568.

Hellevang H. and Aagaard P. (2013) Can the long-term potential for carbonatization and safe long-term CO_2 storage in sedimentary formations be predicted? *Appl. Geochem.* **39**, 108–118.

Hellevang H., Pham V. T. H. and Aagaard P. (2013) Kinetic modelling of CO_2–water–rock interactions. *Int. J. Greenhouse Gas Control* **15**, 3–15.

Hodson M. E. (1999) Micropore surface area variation with grain size in unweathered alkali feldspars: implications for surface roughness and dissolution studies. *Geochim. Cosmochim. Acta* **62**, 3429–3435.

Hodson M. E. (2006) Searching for the perfect surface area normalizing term—a comparison of BET surface area-, geometric surface area- and mass-normalized dissolution rates of anorthite and biotite. *J. Geochem. Explor.* **88**, 288–291.

Knauss K. G., Nguyen S. N. and Weed H. C. (1993) Diopside dissolution kinetics as a function of pH, CO_2, temperature, and time. *Geochim. Cosmochim. Acta* **57**, 285–294.

Lai P., Moulton K. and Krevor S. (2015) Pore-scale heterogeneity in the mineral distribution and reactive surface area of porous rocks. *Chem. Geol.* **411**, 260–273.

Lasaga A. C. (1984) Chemical-kinetics of water–rock interactions. *J. Geophys. Res.* **89**, 4009–4025.

Landrot G., Ajo-Franklin J. B., Yang L., Cabrini S. and Steefel C. I. (2012) Measurement of accessible reactive surface area in a sandstone, with application to CO_2 mineralization. *Chem. Geol.* **318-319**, 113–125.

Li L., Steefel C. I., Williams K. H., Wilkins M. J. and Hubbard S. S. (2009) Mineral transformation and biomass accumulation associated with uranium bioremediation at rifle, Colorado. *Environ. Sci. Technol.* **43**, 5429–5435.

Liu C., Liu Y., Kerisit S. and Zachara J. (2015) Pore-scale process coupling and effective surface reaction rates in heterogeneous subsurface materials. *Rev. Mineral. Geochem.* **80**, 191–216.

Lutterotti L., Matthies S., Wenk H. R., Schultz A. S. and Richardson, Jr., J. W. (1997) Combined texture and structure analysis of deformed limestone from time-of-flight neutron diffraction spectra. *J. Appl. Phys.* **81**, 594–600.

Lutterotti L., Voltolini M., Wenk H.-R., Bandyopadhyay K. and Vanorio T. (2010) Texture analysis of a turbostratically disordered Ca-montmorillonite. *Am. Mineral.* **95**, 98–103.

Maher K., Steefel C. I., DePaolo D. J. and Viani B. E. (2006) The mineral dissolution rate conundrum: insights from reactive transport modeling of U isotopes and pore fluid chemistry in marine sediments. *Geochim. Cosmochim. Acta* **70**, 337–363.

Maher K., Steefel C. I., White A. F. and Stonestrom D. A. (2009) The role of reaction affinity and secondary minerals in regulating chemical weathering rates at the Santa Cruz Soil Chronosequence, California. *Geochim. Cosmochim. Acta* **73**, 2804–2831.

Marini L. (2007) *Geological Sequestration of Carbon Dioxide: Thermodynamics, Kinetics, and Reaction Path Modeling*. Elsevier, Amsterdam.

Marty N., Claret F., Lassin A., Tremosa J. and Blanc P. (2015) A database of dissolution and precipitation rates for clay-rocks minerals. *Appl. Geochem.* **55**, 108–118.

McAdam A. C., Zolotov M. Y., Sharp T. G. and Leshin L. A. (2008) Preferential low-pH dissolution of pyroxene in plagioclase–pyroxene mixtures: implications for Martian surface materials. *Icarus* **196**, 90–96.

McCusker L. B., Von Dreele R. B., Cox D. E., Louër D. and Scardi P. (1999) Rietveld refinement guidelines. *J. Appl. Crystallogr.* **32**, 36–50.

Metz V., Raanan H., Pieper H., Bosbach D. and Ganor J. (2005) Towards the establishment of a reliable proxy for the reactive surface area of smectite. *Geochim. Cosmochim. Acta* **69**, 2581–2591.

Mito S., Xue Z. and Ohsumi T. (2008) Case study of geochemical reactions at the Nagaoka CO_2 injection site, Japan. *Int. J. Greenhouse Gas Control* **2**, 309–318.

Mito S., Xue Z. and Sato T. (2013) Effect of formation water composition on predicting CO_2 behavior: a case study at the Nagaoka post-injection monitoring site. *Appl. Geochem.* **30**, 33–40.

Molins S. (2015) Reactive interfaces in direct numerical simulation of pore-scale processes. *Rev. Mineral. Geochem.* **80**, 461–481.

Navarre-Sitchler A., Steefel C. I., Sak P. B. and Brantley S. L. (2011) A reactive-transport model for weathering rind formation on basalt. *Geochim. Cosmochim. Acta* **75**, 7644–7667.

Nogues J. P., Fitts J. P., Celia M. A. and Peters C. A. (2013) Permeability evolution due to dissolution and precipitation of carbonates using reactive transport modeling in pore networks. *Water Resour. Res.* **49**, 6006–6021.

Noiriel C., Steefel C. I., Yang L. and Ajo-Franklin J. (2012) Upscaling calcium carbonate precipitation rates from pore to continuum scale. *Chem. Geol.* **318–319**, 60–74.

Oelkers E. H. and Gislason S. R. (2001) The mechanism, rates and consequences of basaltic glass dissolution: I. An experimental study of the dissolution rates of basaltic glass as a function of aqueous Al, Si and oxalic acid concentration at 25 C and pH = 3 and 11. *Geochim. Cosmochim. Acta* **65**, 3671–3681.

Oelkers E. H. and Schott J. (1995) Experimental study of anorthite dissolution and the relative mechanism of feldspar hydrolysis. *Geochim. Cosmochim. Acta* **59**, 5039–5053.

Oelkers E. H. and Schott J. (2001) An experimental study of enstatite dissolution rates as a function of pH, temperature, and aqueous Mg and Si concentration, and the mechanism of

pyroxene/pyroxenoid dissolution. *Geochim. Cosmochim. Acta* **65**, 1219–1231.

Palandri J. L., Kharaka Y. K. (2004) A compilation of rate parameters of water–mineral interaction kinetics for application to geochemical modeling (No. 2004–1068). In *US Geol. Surv. Open File Report*.

Park A.-H. A. and Fan L.-S. (2004) CO_2 mineral sequestration: physically activated dissolution of serpentine and pH swing process. *Chem. Eng. Sci.* **59**, 5241–5247.

Peters C. A. (2009) Accessibilities of reactive minerals in consolidated sedimentary rock: an imaging study of three sandstones. *Chem. Geol.* **265**, 198–208.

Pham V. T. H., Lu P., Aagaard P., Zhu C. and Hellevang H. (2011) On the potential of CO_2–water–rock interactions for CO_2 storage using a modified kinetic model. *Int. J. Greenhouse Gas Control* **5**, 1002–1015.

Plummer L. N. and Wigley T. M. L. (1976) The dissolution of calcite in CO_2-saturated solutions at 25 °C and 1 atmosphere total pressure. *Geochim. Cosmochim. Acta* **40**, 191–202.

Pokrovsky O. S. and Schott J. (2000) Kinetics and mechanism of forsterite dissolution at 25 °C and pH from 1 to 12. *Geochim. Cosmochim. Acta* **64**, 3313–3325.

Schott J., Berner R. A. and Sjöberg E. L. (1981) Mechanism of pyroxene and amphibole weathering—I. Experimental studies of iron-free minerals. *Geochim. Cosmochim. Acta* **45**, 2123–2135.

Smith M. M., Wolery T. J. and Carroll S. A. (2013) Kinetics of chlorite dissolution at elevated temperatures and CO_2 conditions. *Chem. Geol.* **347**, 1–8.

Steefel C. I. and Lasaga A. C. (1994) A coupled model for transport of multiple chemical-species and kinetic precipitation dissolution reactions with application to reactive flow in single-phase hydrothermal systems. *Am. J. Sci.* **294**, 529–592.

Steefel C. I. and Lichtner P. C. (1998) Multicomponent reactive transport in discrete fractures: I. Controls on reaction front geometry. *J. Hydrol.* **209**, 186–199.

Steefel C. I. and Van Cappellen P. (1990) A new kinetic approach to modeling water-rock interaction – the role of nucleation, precursors, and Ostwald ripening. *Geochim. Cosmochim. Acta* **54**, 2657–2677.

Steefel C. I., DePaolo D. J. and Lichtner P. C. (2005) Reactive transport modeling: an essential tool and a new research approach for the Earth sciences. *Procedia Earth Planet. Sci.* **240**, 539–558.

Steefel C. I., Beckingham L. E. and Landrot G. (2015a) Micro-continuum approaches for modeling pore-scale geochemical processes. *Rev. Mineral. Geochem.* **80**, 217–246.

Steefel C. I., Appelo C. A. J., Arora B., Jacques D., Kalbacher T., Kolditz O., Lagneau V., Lichtner P. C., Mayer K. U., Meeussen J. C. L., Molins S., Moulton D., Shao H., Šimůnek J., Spycher N., Yabusaki S. B. and Yeh G. T. (2015b) Reactive transport codes for subsurface environmental simulation. *Comput. Geosci.* **19**, 445–478. http://dx.doi.org/10.1007/s10596-014-9443-x.

Stillings L. L. and Brantley S. L. (1995) Feldspar dissolution at 25 C and pH 3. Reaction stoichiometry and the effect of cations. *Geochim. Cosmochim. Acta* **59**, 1483–1496.

Stockmann G. J., Wolff-Boenisch D., Gislason S. R. and Oelkers E. H. (2013) Do carbonate precipitates affect dissolution kinetics? *Chem. Geol.* **337–338**, 56–66.

Sverdrup H. U. (1990) *The Kinetics of Base Cation Release due to Chemical Weathering*. Lund University Press, Lund.

Teng H. H., Dove P. M. and De Yoreo J. J. (2000) Kinetics of calcite growth: surface processes and relationships to macroscopic rate laws. *Geochim. Cosmochim. Acta* **64**, 2255–2266.

Tester J. W., Worley W. G., Robinson B. A., Grigsby C. O. and Feerer J. L. (1994) Correlating quartz dissolution kinetics in pure water from 25 to 625 C. *Geochim. Cosmochim. Acta* **58**, 2407–2420.

Walter L. M. and Morse J. W. (1984) Reactive surface area of skeletal carbonates during dissolution: effect of grain size. *J. Sediment. Res.* **54**, 1081–1090.

Weibel E. R. (1979) *Stereological Methods*. Academic Press, London.

White S. P., Allis R. G., Moore J., Chidsey T., Morgan C., Gwynn W. and Adams M. (2005) Simulation of reactive transport of injected CO_2 on the Colorado Plateau, Utah, USA. *Chem. Geol.* **217**, 387–405.

White A. F., Schulz M. S., Vivit D. V., Blum A. E., Stonestrom D. A. and Anderson S. P. (2008) Chemical weathering of a marine terrace chronosequence, Santa Cruz, California I: interpreting rates and controls based on soil concentration-depth profiles. *Geochim. Cosmochim. Acta* **72**, 36–68.

Wieland E. and Stumm W. (1992) Dissolution kinetics of kaolinite in acidic aqueous solutions at 25 C. *Geochim. Cosmochim. Acta* **56**, 3339–3355.

Wigley M., Dubacq B., Kampman N. and Bickle M. (2013) Controls of sluggish, CO_2-promoted, hematite and K-feldspar dissolution kinetics in sandstones. *Earth Planet. Sci. Lett.* **362**, 76–87.

Xu T., Apps J. A. and Pruess K. (2004) Numerical simulation of CO_2 disposal by mineral trapping in deep aquifers. *Appl. Geochem.* **19**, 917–936.

Xu T., Yue G., Wang F. and Liu N. (2014) Using natural CO_2 reservoir to constrain geochemical models for CO_2 geological sequestration. *Appl. Geochem.* **43**, 22–34.

Zerai B., Saylor B. Z. and Matisoff G. (2006) Computer simulation of CO_2 trapped through mineral precipitation in the Rose Run Sandstone, Ohio. *Appl. Geochem.* **21**, 223–240.

Zhang W., Li Y., Xu T., Cheng H., Zheng Y. and Xiong P. (2009) Long-term variations of CO_2 trapped in different mechanisms in deep saline formations: a case study of the Songliao Basin, China. *Int. J. Greenhouse Gas Control* **3**, 161–180.

Zhang R., Zhang X., Guy B., Hu S., De Ligny D. and Moutte J. (2013) Experimental study of dissolution rates of hedenbergitic clinopyroxene at high temperatures: dissolution in water from 25 C to 374 C. *Eur. J. Mineral.* **25**, 353–372.

Zhu C. and Lu P. (2013) The coupling of dissolution and precipitation reactions as the main contributor to the apparent field-lab rate discrepancy. *Procedia Earth Planet. Sci.* **7**, 948–952.

Associate editor: Caroline Peacock